



Intricate heterogeneous structures of the top 300 km of the Earth's inner core inferred from global array data: II. Frequency dependence of inner core attenuation and its implication



R. Iritani¹, N. Takeuchi, H. Kawakatsu*

Earthquake Research Institute, The University of Tokyo, 1-1-1 Yayoi, Bunkyo-ku, Tokyo 113-0032, Japan

ARTICLE INFO

Article history:

Received 21 May 2014

Received in revised form 25 August 2014

Accepted 27 August 2014

Available online xxx

Editor: P. Shearer

Keywords:

inner core

attenuation

simulated annealing

waveform inversion

frequency dependence

absorption band model

ABSTRACT

We apply a nonlinear waveform inversion method that we developed previously (Iritani et al., 2010, 2014) to broadband (0.02–2 Hz) core phase data recorded by global seismic arrays in order to investigate the frequency dependence of inner core attenuation. The results show a prominent difference of the frequency dependence of attenuation between the eastern hemisphere and the western hemisphere: while attenuation is frequency dependent in the western hemisphere, not so in the eastern hemisphere. Moreover, in the western hemisphere, a stronger frequency dependence of the attenuation is observed beneath Africa compared to beneath North America. This intricate quasi-hemispherical property of the frequency dependence of the inner core attenuation, together with the quasi-hemispherical variability of seismic velocity and attenuation strength at around 1 Hz that we reported earlier, can be consistently understood in terms of the relative location of the seismic observation frequency band and the absorption band peaks that are different for regions. The variability of the absorption band peak may reflect the variability of the iron grain size of the inner core: the grain size is larger in the eastern hemisphere than the western hemisphere, and in the western hemisphere beneath North America, it gradually increases with depth. However, caution should be taken in this inference as the physical mechanism of attenuation in the inner core is still poorly constrained both theoretically and observationally.

© 2014 Elsevier B.V. All rights reserved.

1. Introduction

The seismologically inferred hemispherical heterogeneity of the inner core, in which the eastern hemisphere shows high attenuation and faster velocity and the western hemisphere shows low attenuation and slower velocity near the surface (Tanaka and Hamaguchi, 1997; Wen and Niu, 2002; Cao and Romanowicz, 2004; Yu and Wen, 2006; Tanaka, 2012), has been considered as one of the most important constraints for delineating the solidification process of the inner core. Although several hypotheses, such as a large scale flow of the outer core arisen by the heterogeneous heat flux at the CMB (Sumita and Olson, 1999; Aubert et al., 2008; Gubbins et al., 2011), and a convective transition of grain growth from crystallizing side in the eastern hemisphere to melting side in the western hemisphere (Monnereau et al., 2010; Alboussière et al., 2010), are proposed for the origin, two schools of models

predict different and nearly opposite regions of crystallizing and melting of the inner core, which may be resolved via seismological means (e.g., Cormier and Attanayake, 2013). Recently, Attanayake et al. (2014) and Iritani et al. (2014) reported the presence of more complex structures than the previously suggested hemispherical heterogeneity. In Iritani et al. (2014) (hereafter, paper 1), by analyzing short period core phase data (~1 Hz) recorded by the global seismic arrays, we reported the existence of a small-scale heterogeneity of attenuation in the western hemisphere of the top 300 km of the inner core and the absence of the heterogeneity below the 300 km depth, which may indicate more complex growth mechanism of the inner core. To further provide constraints on the reported structures, in this study, we focus on the frequency dependence of attenuation and velocity structure of the inner core.

Doornbos (1983) analyzed the core-phase data passing from Fiji to NORSAR by employing the absorption band theory (e.g. Liu et al., 1976), and suggested that frequency dependent attenuation (Q_p^{-1}) existed for frequencies of 0.5–2 Hz and the lower cut-off frequency of the absorption band is located above 2 Hz. By comparing high-frequency (1–5 Hz) PKP(CD) and PKP(DF) phases for Indonesia–North American paths, Cummins and Johnson (1988)

* Corresponding author.

¹ Now at Schlumberger K. K., 2-2-1 Fuchinobe, Chuo-ku, Sagami-hara, Kanagawa 252-0206, Japan.

supported Doornbos's observation with a noted trade-off with the inner core P-wave velocity. Cormier et al. (1998) and Li and Cormier (2002), who analyzed global core phase data for a distance range of 150–180°, also demonstrated the frequency dependent attenuation over a broader frequency range (0.02–2 Hz), although they did not confirm the hemispherical variation of the attenuation. In contrast, Bhattacharyya et al. (1993) and Souriau and Roudil (1995) analyzed spectral amplitude ratios between PKP(DF) and PKP(BC) for globally observed data filtered with corner frequencies of 0.2–1.5 Hz and 0.2–2 Hz, respectively, and concluded that the attenuation of the inner core is not frequency dependent. Recently, the existence of anisotropy of the frequency dependent attenuation has been suggested. Souriau (2009) has shown that the variation of amplitude ratios between PKP(DF) and PKP(BC) is strongly dependent on the angle of the ray path from the earth's rotation axis by analyzing the data that sample the inner core beneath Africa. Cormier and Li (2002) also revealed that the anisotropy of the frequency dependent attenuation under the assumption of the frequency dependent attenuation that is attributable to scattering by the heterogeneous fabric, and concluded that these features can be explained by varying the scale length of the fabric within a range of 1–10 km.

Existence or absence of the frequency dependence of attenuation of the inner core, therefore, does not appear to have achieved a consensus among scientists. There also exists no conclusive evidence for the hemispherical heterogeneities of the frequency dependence of the inner core attenuation. In this paper, we extend the waveform inversion approach that we developed previously (Iritani et al., 2010, 2014), where we applied for short-period data, such that the frequency dependence of the inner core attenuation can be incorporated, and apply it to data of broadband seismic arrays deployed globally. By consistently modeling broadband waveforms with inclusion of variable velocity dispersion effect (equivalent to the frequency dependent attenuation), we show that the previously reported quasi-hemispheric velocity and attenuation variations at a reference frequency (1 Hz) (Iritani et al., 2014) can be understood in terms of the regional variations of the relative location of the absorption band to the seismic frequency band of analysis. With this view, the positive correlation between attenuation and seismic velocity variations in the inner core, often noted as a line of supporting evidence for the scattering origin of attenuation (e.g., Souriau, 2003; Monnerieu et al., 2010), can be explained as a natural consequence of frequency shift of the absorption band. We further attempt to interpret this observation to infer the growth process of the inner core.

2. Method of data analysis

2.1. Method of waveform inversion for frequency dependent attenuation

2.1.1. Parameterization of waveforms with frequency dependent Q^{-1}

We employ the waveform inversion method used in our previous studies (Iritani et al., 2010, 2014). In the method, three core phases, PKP(DF), PKP(BC) and PKP(AB) of each record section, are modeled by one reference waveform that represents an incident waveform to the array and by parameters for each phase, such as traveltime, amplitude and attenuation parameter of the inner core: a model waveform for a station i is then defined by

$$S_i(t) = R_i^{DF} A(t_i^{*DF}) * W(t - \tau_i^{DF}) + R_i^{BC} W(t - \tau_i^{BC}) + R_i^{AB} H * W(t - \tau_i^{AB}) \quad (1)$$

where $W(t)$ is the time series of the reference waveform, $A(t^*)$ is the attenuation operator, H and the asterisk respectively denote the Hilbert transform and a convolution, and τ , R , and t^*

are the traveltime, amplitude correction, and attenuation parameter of each core phase indicated by the superscript, respectively. Optimal parameters that explain observed waveforms best are obtained by using the simulated annealing algorithm (Chevrot, 2002; Garcia et al., 2004, 2006; Iritani et al., 2010, 2014).

In our previous studies, we assumed that Q^{-1} had no frequency dependence, and used t^* as the parameter that defines the strength of attenuation along the ray path. In this study, we modify the attenuation operator in Eq. (1) by introducing frequency dependent attenuation (or Q^{-1} ; note that we use words attenuation and Q^{-1} interchangeably for the same meaning when we discuss their frequency dependence). The attenuation operator for a wave that passes through a material with a frequency dependent velocity, $\alpha(\omega)$, is obtained by the solution of the wave equation, and is written as follows in the frequency domain:

$$A(t) = \int \exp\left[-i\omega \int_{\text{Path}} \left(\frac{1}{\alpha(\omega)} - \frac{1}{\alpha_0}\right) dS\right] d\omega. \quad (2)$$

We employ the absorption band model defined by Cormier and Richards (1988), and the dispersion relation for P-wave is given by the following function:

$$\alpha(\omega) = \alpha_0 \frac{[1 + (2/\pi) Q_m^{-1} D(\omega)]^{1/2}}{\text{Re}[1 + (2/\pi) Q_m^{-1} D(2\pi)]^{1/2}} \left(D(\omega) = \ln \left[\frac{i\omega + (1/\tau_1)}{i\omega + (1/\tau_2)} \right] \right), \quad (3)$$

where α_0 is the velocity at 1 Hz, Q_m^{-1} is the maximum value of attenuation, and τ_1 and τ_2 represent the lower and higher corner frequencies of an absorption band, respectively (the corresponding corner frequencies are $f_1 = 1/(2\pi\tau_1)$ and $f_2 = 1/(2\pi\tau_2)$). (The denominator of (3) is slightly different from those in Cormier and Richards (1988) and Li and Cormier (2002) which seem to have a typo.)

The attenuation as a function of frequency is given by

$$Q^{-1}(\omega) = 2 \frac{\text{Im}[\alpha(\omega)]}{\text{Re}[\alpha(\omega)]}. \quad (4)$$

The peak attenuation, Q_m^{-1} , is related to Q^{-1} at 1 Hz, $Q_{1\text{Hz}}^{-1}$ as follows:

$$Q_m^{-1} = \frac{2\pi Q_{1\text{Hz}}^{-1} \text{Im}(D(\omega))}{[(Q_{1\text{Hz}}^{-1})^2 - 4] \text{Im}(D(\omega))^2 + 4 Q_{1\text{Hz}}^{-1} \text{Im}(D(\omega)) \text{Re}(D(\omega))}. \quad (5)$$

Fig. 1a presents an example of the absorption band model. Note that the constant Q^{-1} roughly corresponds to the frequency dependent velocity (dispersion), and the frequency dependent Q^{-1} does so to the constant velocity (no dispersion).

Note that the width of the absorption band is defined by the ratio τ_1/τ_2 , and we fix it as $\tau_1/\tau_2 = 10^5$ following Liu et al. (1976) and Li and Cormier (2002). Considering the band width of seismic observation is quite limited (0.02–2 Hz), this restriction has almost no effect on the result (Li and Cormier, 2002), and we effectively have two parameters, τ_1 and $Q_{1\text{Hz}}$, for the attenuation operator (as opposed to one in the frequency independent attenuation case). The model waveform in (1) is then modified as

$$S_i(t) = R_i^{DF} A(Q_{1\text{Hz}i}^{-1}, \tau_{1i}) * W(t - \tau_i^{DF}) + R_i^{BC} W(t - \tau_i^{BC}) + R_i^{AB} H * W(t - \tau_i^{AB}). \quad (6)$$

In Liu et al. (1976), the absorption band attenuation model is suggested on the basis of the intrinsic attenuation specified by the relaxation time. For the case of scattering, attenuation has a peak

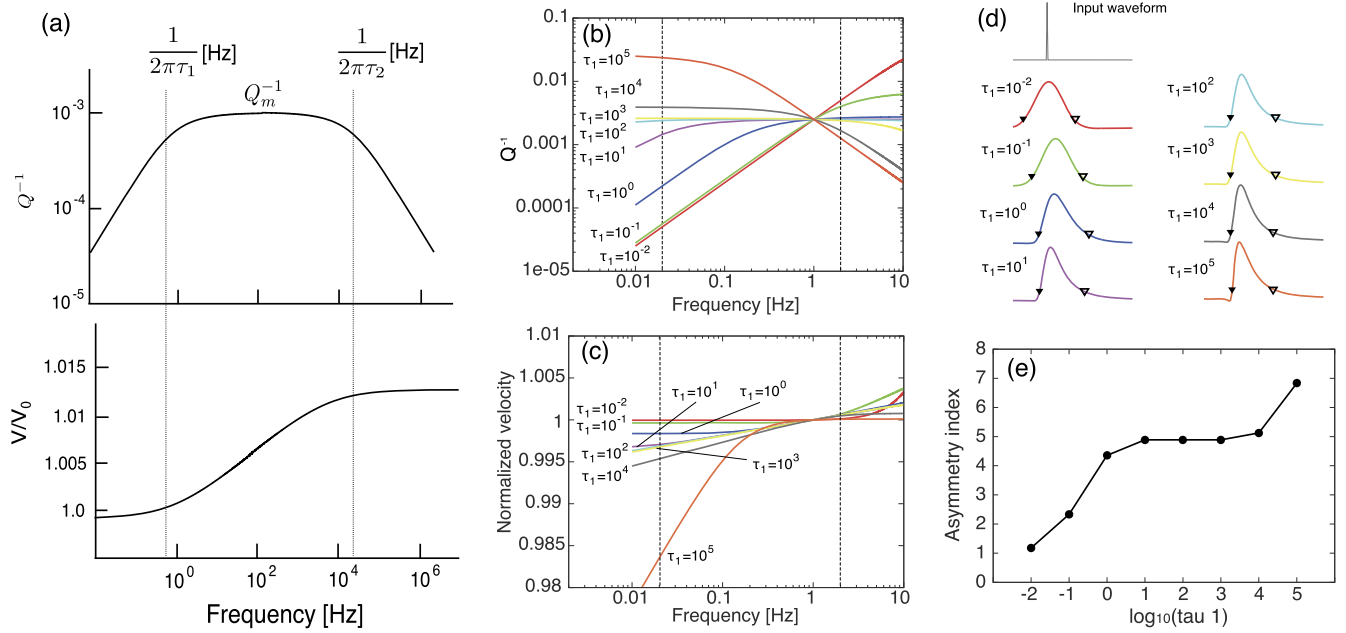


Fig. 1. (a) The absorption band model ($Q^{-1}(\omega)$, $\alpha(\omega)$) employed in this study (a case for $\tau_1 = 10^0$, $Q_m^{-1} = 10^{-3}$). (b) Attenuation spectra and (c) velocity dispersion curves for the eight absorption band models. (d) Impulse responses of the eight absorption band models that share a similar RMS amplitude. Arrows represent points at which the amplitude is 10% of the peak amplitude. (e) The ratio of the time lengths before and after the peak (asymmetric index). (For interpretation of the references to color in this figure, the reader is referred to the web version of this article.)

when the size of scatterers is comparable to the seismic wavelength, and becomes smaller with receding from the peak (Cornier and Li, 2002; Calvet and Margerin, 2008). So the presence of a flat attenuation peak in scattering implies that the distribution of scatterers is self-similar over some scale ranges.

2.1.2. Parameter search with the simulated annealing

As the inclusion of two parameters, τ_{1i} and $Q_{1\text{Hz}i}^{-1}$, as unknown parameters for individual waveforms makes the inversion difficult, we apply the waveform inversion using Eq. (6) for eight absorption band models with pre-set τ_1 ($\tau_1 = 10^{-2}, 10^{-1}, 10^0, 10^1, 10^2, 10^3, 10^4, 10^5$) for each event–array dataset. Fig. 1b, c shows the eight absorption band models used in this study that have the same $Q_{1\text{Hz}}^{-1}$. In the frequency band of interest (0.02–2.0 Hz), the models of $\tau_1 = 10^{-2}$ and 10^{-1} exhibit strongly frequency dependent Q^{-1} ; the model of $\tau_1 = 10^0$ shows frequency dependent Q^{-1} below 1 Hz; the models of $\tau_1 = 10^1$ – 10^3 have nearly constant Q^{-1} , and the models of $\tau_1 = 10^4$ and 10^5 have frequency dependent Q^{-1} above 1 and 0.1 Hz, respectively. Fig. 1d compares impulse responses of the eight absorption band models that share a similar RMS amplitude, and points of 10% of the maximum amplitude are indicated by arrows. Fig. 1e shows that the ratio of the time lengths between the arrows and the peak (referred to as asymmetric index) strongly depends on the choice of an absorption band, i.e., τ_1 .

As for the specific algorithm for the simulated annealing, the only difference from our previous studies (Iritani et al., 2010, 2014) will be mentioned. For given τ_1 , the unknown parameter of the attenuation is $Q_{1\text{Hz}}^{-1}$. A random perturbation to $Q_{1\text{Hz}}^{-1}$ is given by

$$Q_{1\text{Hz}}^{-1} = 0.0001n_Q \quad (0.0001 < Q_{1\text{Hz}}^{-1} < 0.01) \quad (7)$$

where n_Q is an integral uniform random number with which $Q_{1\text{Hz}}^{-1}$ stays in the search range indicated in the parentheses.

After the waveform inversion analysis for eight absorption band models with different τ_1 , eight optimal waveforms are obtained for each trace. As the difference in optimal waveforms due to different attenuation models is restricted to PKP(DF) phases, the summation

of L1 norm of residual waveforms (i.e., misfit) of PKP(DF) phases is used as a measure of the model goodness. This waveform inversion is performed 10 times with different random seeds, and the average and standard deviation of misfits are estimated.

2.2. Test with synthetic and observed waveforms

We first test the resolvability of different absorption band models by analyzing synthetic waveforms. Synthetic waveforms are computed for the VMOI velocity model (Kaneshima et al., 1994) and the PREM attenuation model (Dziewonki and Anderson, 1981) using the DSM (Kawai et al., 2007) modified for frequency dependent attenuation (using Eq. (3)). The synthetic data sets computed for two values of τ_1 ($\tau_1^S = 10^0, 10^2$, where the superscript S denotes the input τ_1 to be distinguished from the inversion parameter) are used, and each data set is composed of 15 waveforms for epicentral distances of 145–152° (Fig. 2a). In the test, we analyze two types of data: velocity and displacement waveforms after applying the same band-pass filter as employed in the data analysis below.

The results are shown in Fig. 2. For the velocity data, there is no resolution among the models of $\tau_1 = 10^0, 10^1, 10^2, 10^3$ (gray lines in Fig. 2c and Fig. 2d). On the other hand, for the displacement data, differences between $\tau_1 = 10^0$ and $\tau_1 = 10^2$ are well resolved (black lines in Fig. 2c and Fig. 2d) although the resolution is still poor for the latter case.

The test indicates the importance of analyzing displacement waveforms in order to resolve presence or absence of the frequency dependence of attenuation for the frequency range of analysis (0.02–2 Hz). Compared to velocity waveforms, more weight is given at lower frequencies for displacement waveforms. While the attenuation spectrum for $\tau_1 = 10^0$ (blue line in Fig. 1b) is frequency dependent below 0.2 Hz and almost constant above 0.2 Hz, those for $\tau_1 = 10^1, 10^2, 10^3$ are constant throughout the frequency range of analysis (Fig. 1b). The difference in the absorption spectra is reflected in waveforms as demonstrated by means of the asymmetric indices (Fig. 2b).

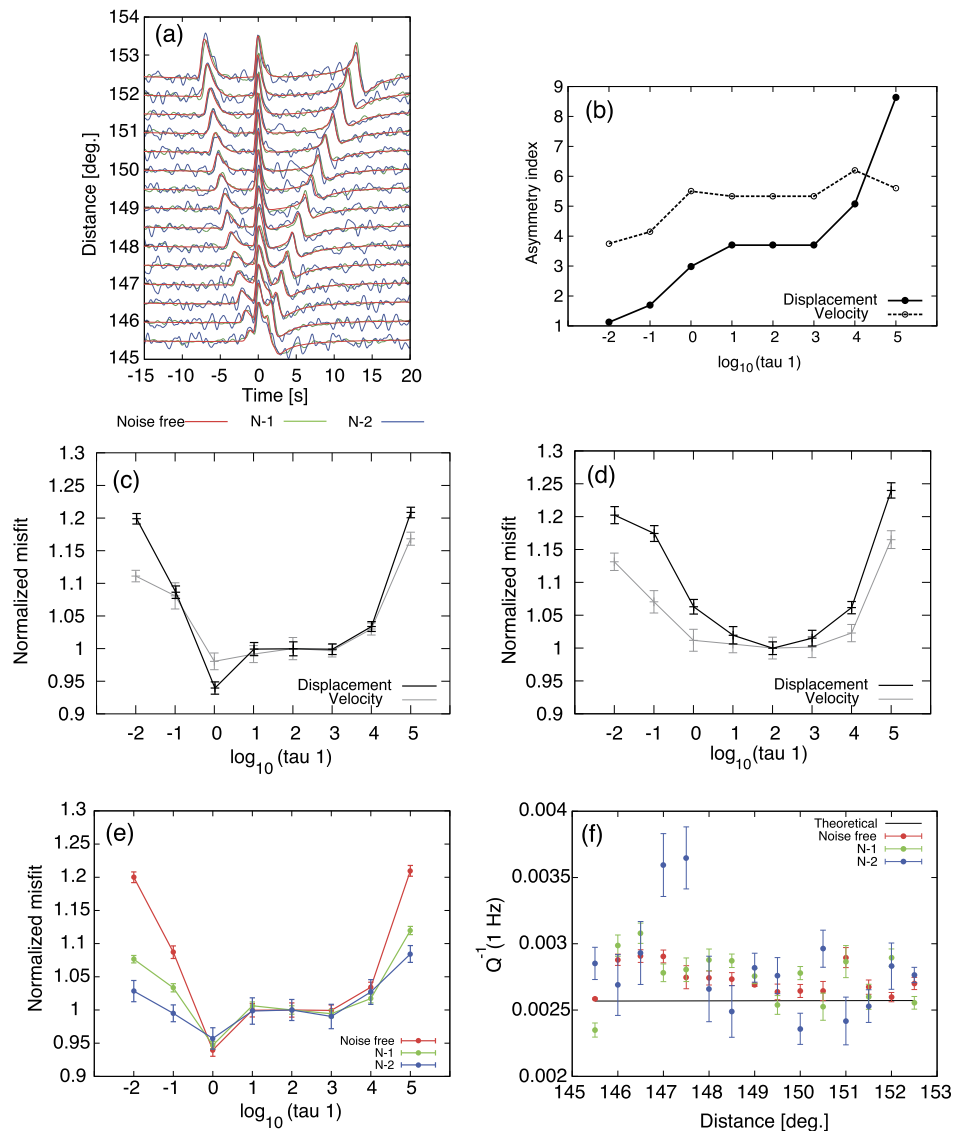


Fig. 2. (a) An example of synthetic section (displacement) for a distance range of 145.5–152.5° ($\tau_1^S = 10^0$). Red, green and blue lines are for noise free, noise level estimated from pre-PKP(DF) waveforms in data (N-1), and one from misfits (N-2; more detail in the text) cases, respectively. (b) Asymmetry indices of noise-free synthetic PKP(DF) waveforms (broken line: velocity; solid line: displacement) at 151.0° calculated for eight attenuation models. Note that the index for displacement waveforms varies significantly for different models. ((c), (d)) Misfit normalized by that of the constant Q^{-1} model (i.e., $\tau_1 = 10^2$): cases for $\tau_1^S = 10^0$ for displacement (black) and velocity (gray) waveforms (c), and cases for $\tau_1^S = 10^2$ (d). (e) Comparison of misfit for noise added displacement synthetics for a case $\tau_1^S = 10^0$. Due to the normalization scheme as in (c, d), error bars are also normalized, resulting in small values for N-1. Colors are the same as in (a). (f) Optimum Q^{-1} (1 Hz) values estimated for individual waveforms. The horizontal black line is the input value, and colors are the same as in (a). Comparing with Fig. S1a, note that the scattered range is relatively small. (For interpretation of the references to color in this figure legend, the reader is referred to the web version of this article.)

To further examine the effect of noise in data, we extended the tests adding white noise in synthetics. As to the noise level, we consider two cases: in the first case, we use the pre-PKP noise level that represents the background noise level of data and is estimated from the average value of the entire dataset (green lines in Fig. 2a). In the second case, which offers a more severe test, we employ a noise level estimated from the maximum RMS of the misfit residual waveforms of the entire dataset (blue lines in Fig. 2a). In both cases, the test results indicate that the model difference is still resolvable, although the difference of misfits is reduced (Fig. 2e). The estimated $Q_{1\text{Hz}}^{-1}$ values are consistent with the input values (Fig. 2f), although there is more scatter for larger noise level cases (the slight bias in $Q_{1\text{Hz}}^{-1}$ estimation toward larger values that exist even for the noise free case is likely due to that the fact that DSM synthetic waveforms have a sharp cut-off at 2 Hz while model waveforms have a more gentle cut-off. See also Fig. S1).

In Fig. 3, we show a typical result for an observed displacement waveform. The contour plot of the misfit function shows a well defined minimum. A small secondary minimum may exist to fit a part before or after the peak better than the other, but it does not seem to affect the global minimum search by the simulated annealing. The situation might be different in the case of Li and Cormier (2002) (their Fig. 7) that exhibits multiple peaks. We attribute the difference partly to the usage of the displacement waveform and partly to fitting the full cycle of the DF waveform (compared to the modeling of the first-half cycle of velocity waveforms (Li and Cormier, 2002; Cormier and Li, 2002)). Kaelin and Johnson (1998), in their work of scattering simulation for 3D heterogeneities, suggest the importance of modeling the full waveform to correctly resolve the dispersion effect. Our approach should be also more robust as our reference waveform, $W(t)$, which is determined from array data, does not suffer much from the source directivity effect.

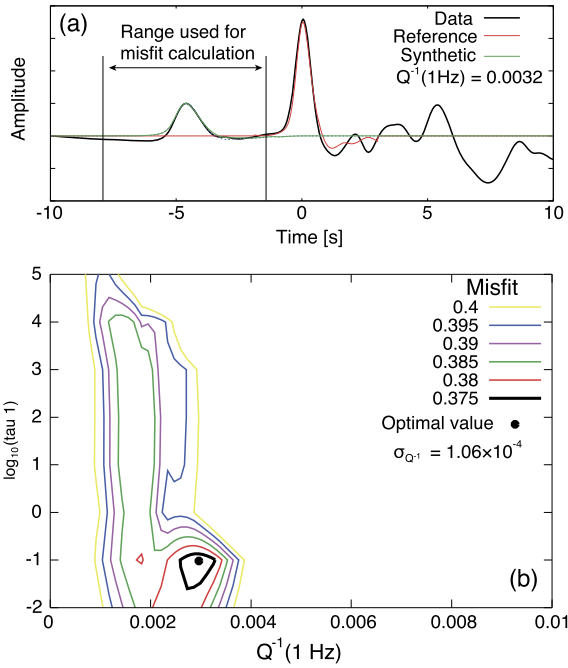


Fig. 3. A typical example of contour plots of misfits calculated for PKP(DF) waveform. The misfit function shows a well-defined global minimum.

2.3. Data

We use the vertical component of broadband core phase data observed by globally deployed broadband seismic arrays (Japanese F-net, NECESSArray, permanent European stations, USArray and PASSCAL arrays), and the information of analyzed events is listed

in paper 1. The angle of the ray paths with respect to the earth’s rotation axis is greater than 40° (i.e., equatorial paths) for all data sets used in this study, and the effect of anisotropy of the inner core is not significant. We analyze only those waveforms that contain both DF and BC phases. We apply the second order zero-phase Butterworth band-pass filter with corner frequencies of 0.02 and 2 Hz. In paper 1, we showed that two representative regional 1-D attenuation structures existed in the western hemisphere: W1 beneath Africa and W2 beneath the north American continent. We, therefore, analyze data from these two areas separately. The distribution of events, stations and ray paths within the inner core, and the areas of W1 and W2 are shown in Fig. 4a.

3. Results

Fig. 5 shows examples of the data analysis for each of the three regions: each column corresponds to one event–array data. The misfits (Fig. 5a, e, i) indicate that different attenuation models ($\tau_1 = 10^1, 10^0, 10^{-1}$) are best for different regions. The second row (Fig. 5b, f, j) compares observed PKP(DF) waveforms with optimal model waveforms for the three τ_1 models, showing that the minimum misfit model always fit the waveform best.

As shown in Fig. 1d, attenuation operator waveforms change with τ_1 , and it results in a tradeoff between measurements of $Q_{1\text{Hz}}^{-1}$ and traveltime. To consider this effect, we compare the obtained $Q_{1\text{Hz}}^{-1}$ and traveltime in this study with those measured by analyzing the narrow band-pass filtered data (0.35–2 Hz) in paper 1. In paper 1, we measured t^* at around 1 Hz for the same data sets that are analyzed in this study. We convert t^* to $Q_{1\text{Hz}}^{-1}$ by using the following equation:

$$Q_i^{-1}(1\text{ Hz}) = \frac{t^*}{T_i} \tag{8}$$

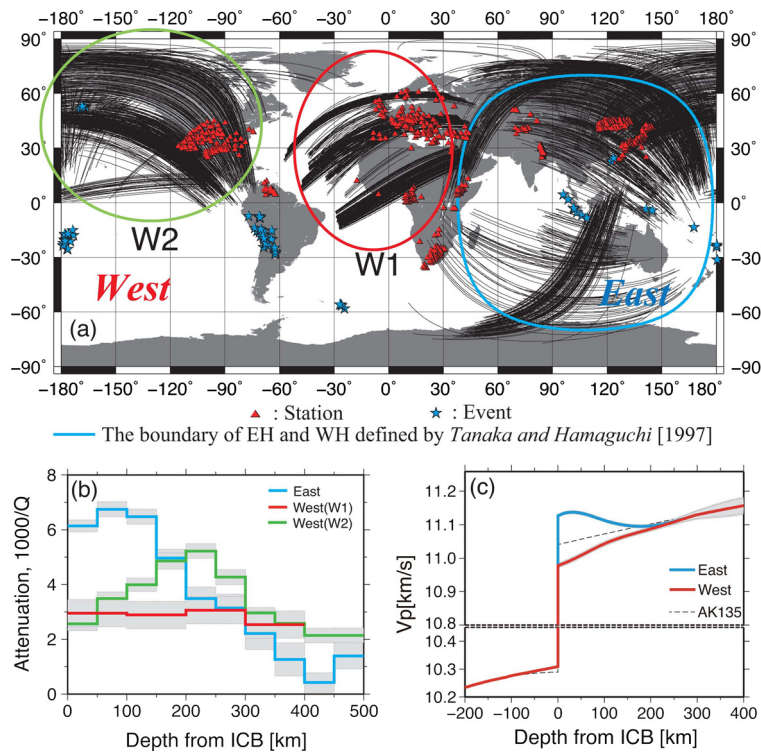


Fig. 4. (a) The distribution of stations (red triangle), events (blue star) and ray paths of core phases (black line) that are used in this study. The blue line indicates the boundary between the eastern and western hemispheres defined by Tanaka and Hamaguchi (1997), and the inside of the blue circle corresponds to the eastern hemisphere; the red and green circles indicate two areas (W1 and W2) in the western hemisphere that show different attenuation structures as in (b). (b) Attenuation profiles for the top 500 km and (c) velocity profiles for the top 400 km of the inner core obtained by analyzing short period data (the dominant frequency of 1 Hz) in paper 1. The model errors are shown by the gray shadow. (For interpretation of the references to color in this figure legend, the reader is referred to the web version of this article.)

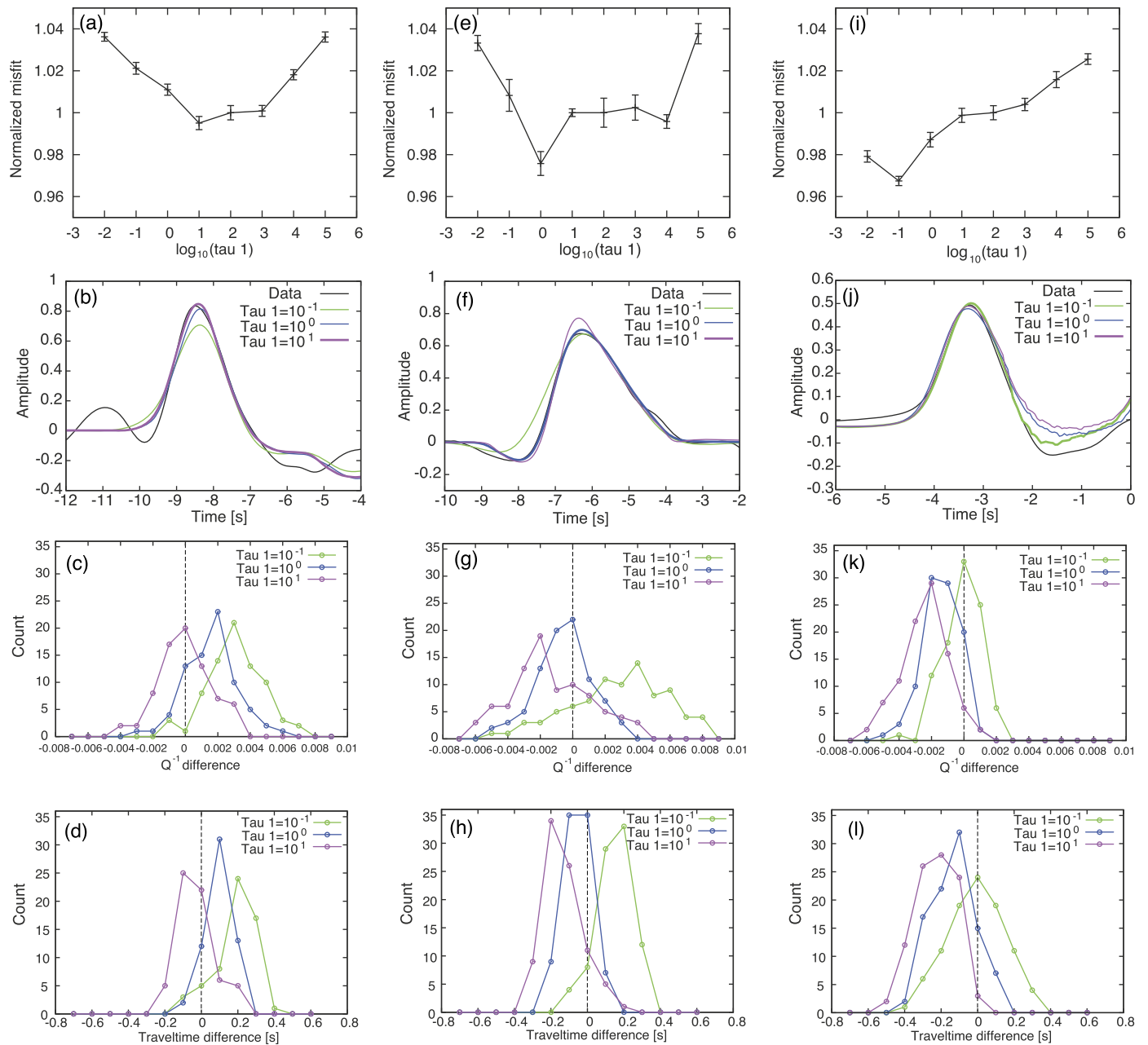


Fig. 5. Examples of the results for event-array pairs (a)–(d) for the eastern hemisphere, (e)–(h) for the western hemisphere (W2) and (i)–(l) for the western hemisphere (W1). The first row ((a), (e), (i)) shows the L1 norm misfits for different τ_1 models. The second row ((b), (f), (j)) compares PKP(DF) waveforms of the data and optimal model waveforms. The third row ((c), (g), (k)) shows histograms of the difference between $Q_{1\text{Hz}}^{-1}$ for different τ_1 in this study and Q^{-1} for short period data obtained in paper 1. The fourth row ((d), (h), (l)) shows the same as above but for travel times. Note that the models with the smallest misfits (first row) exhibit peaks at zero difference in the histograms (third and fourth rows).

where T_i is the traveltime in the inner core for the i -th path. The results shown in the third and fourth rows (Fig. 5c, g, k and d, h, l) indicate that the best models always give consistent $Q_{1\text{Hz}}^{-1}$ and traveltimes with those measured in paper 1, suggesting internal consistency of our modeling.

Fig. 6a shows histograms of the best τ_1 values for three regions. For the eastern hemisphere, a peak is at $\tau_1 = 10^1$, and frequency independent attenuation models (i.e., $\tau_1 = 10^{1,2,3}$) are selected as the best model in almost all data (see also Fig. 2). On the other hand, the results for W1 and W2 have peaks at $\tau_1 = 10^{-1}$ and $\tau_1 = 10^0$, respectively; i.e., the frequency dependence of attenuation exists beneath W1, and the attenuation beneath W2 is constant at high frequencies (~ 1 Hz) and frequency dependent at low

frequencies (< 0.1 Hz). Fig. 6b and Fig. 6c show corresponding best absorption band model spectra for three regions.

The absence or presence of the frequency dependence of attenuation should reflect in waveforms as velocity dispersion (Fig. 1d). Here we show that the difference of dispersion can be well observed in stacked waveforms for three studied regions which show different attenuation spectra (Fig. 6b, c). Fig. 7a shows PKP(DF)s for three regions stacked for all analyzed data after deconvolved by the inverted reference waveform for each record section. While the stacked waveform for the eastern hemisphere shows a long-tailed feature (blue line), the others show more symmetric shape (green for W2, red for W1). (Fig. 7b shows a similar plot for PKP(BC)s. Note that waveforms are all symmetric for different regions.) The same is true for one-degree-binned stacked waveforms as shown

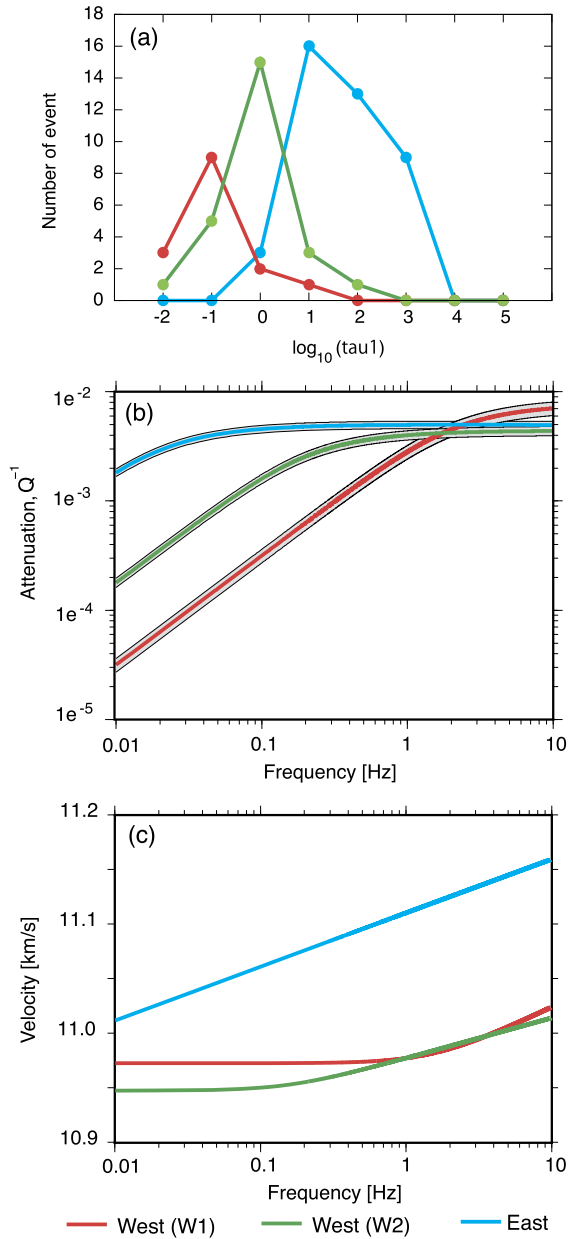


Fig. 6. (a) Histograms of optimal absorption models for three regions. Best absorption models for three regions are shown (b) in attenuation spectra, and (c) in dispersion curves.

below in a different way. In Fig. 7c, the asymmetry indexes of the theoretical impulse response functions are estimated for eight absorption band models with varying $Q_{1\text{Hz}}^{-1}$, and compared with those of the observed one-degree-binned stacked source-deconvolved PKP(DF) waveforms. Note that the measured indexes and $Q_{1\text{Hz}}^{-1}$ for each region are grouped together confirming the aforementioned waveform characteristics. Also those measured values are consistent with the best absorption band models estimated for each region in this paper (Fig. 6).

Fig. 8 further shows comparison of individual waveforms for each region at several representative distances. Although direct comparisons of observed (filtered) records and modeled ones (convolved with corresponding reference waveform) show, by visual inspection, subtle difference for different parameters, τ_1 (Fig. 8a–c), both residual waveforms and misfit functions (Fig. S2) indicate the preferred τ_1 values for each region consistently give the best fit. Fig. 8d also compares PKP(DF) phases, after deconvolved by

the optimal reference waveforms, for individual records. Similar to Fig. 7a, individual records also show the different waveform characteristics for different regions confirming the aforementioned results.

4. Discussion

4.1. Comparison with the previous studies

The result of our analysis for the frequency dependence of attenuation in the inner core is consistent with some of previous studies, but not with all of them. Our result can be considered consistent with those of Bhattacharyya et al. (1993) and Souriau and Roudil (1995) who analyzed global data by employing the spectral ratio technique and reported frequency independence of attenuation. In their analyses, a narrower band-pass filter (0.2–2 Hz) than our analysis was applied to the data. In this frequency range, our result for W2 shows nearly constant Q^{-1} (Fig. 6b). Considering that the number of the data sampling the region W1, which show frequency dependent attenuation here, is quite limited in their analyses (none in Bhattacharyya et al. (1993) and about 10% in Souriau and Roudil (1995)), the feature of frequency independent attenuation is likely to have dominated in their results. It should be also noted that the spectral ratio technique is less robust, compared to the waveform inversion employed here (also, Li and Cormier, 2002; Cormier and Li, 2002) or a method that directly measures the effect of velocity dispersion (e.g., Doornbos, 1983), to delineate the frequency dependence/independence of attenuation, as it potentially suffers from biases introduced by strong spectral peaks and troughs in a relatively narrow band that affects the results of linear regression of log of spectral ratios.

Our result, on the other hand, appears not consistent with that of Doornbos (1983) who reported frequency dependent attenuation and absence of velocity dispersion for the Fiji-NORSAR path which is classified here as in the eastern hemisphere near the boundary. Souriau and Roudil (1995) also reported though not conclusive, via spectral division, that a similar feature existed for paths from the south-west Pacific to Europe as “a notable exception”. As Doornbos (1983)’s original observation is based mainly on the two observations: “anomalously weak” (1) high-frequency components and (2) dispersion in PKP(DF) waveforms, we argue that Doornbos’s observation is consistent with our model which indicates strong attenuation and fast velocity at a reference frequency, 1 Hz, in the shallow part of the eastern hemisphere of the inner core as follows. If we were to estimate the arrival time of a high-frequency (say 1 Hz) DF-phase assuming an average structure which might have been available in 1980’s, it would be delayed compared to the reality that is now well established as the hemispherical heterogeneity. If the low-frequency DF-phase experiences relatively slow velocity, as in our model for the eastern hemisphere, both high- and low-frequency components might be interpreted to arrive in close time that would be considered as a result of weak dispersion. So Doornbos’s observation, which was interpreted without the knowledge of the lateral heterogeneity of the inner core, can be considered consistent with our model (and observation). This thought experiment also demonstrates the importance of estimating structures at an appropriate reference frequency using an internally consistent approach as done in this study. Similarly, the result of Cummins and Johnson (1988), who supported Doornbos’s observation of frequency dependent attenuation for paths from western Pacific to north America that belong to the eastern hemisphere, can be also considered consistent with our result. As they note, their analysis, which is based on short-period (1–5 Hz) records, shows a trade-off with the P-wave velocity at the top of the inner core that is now known to be faster in the

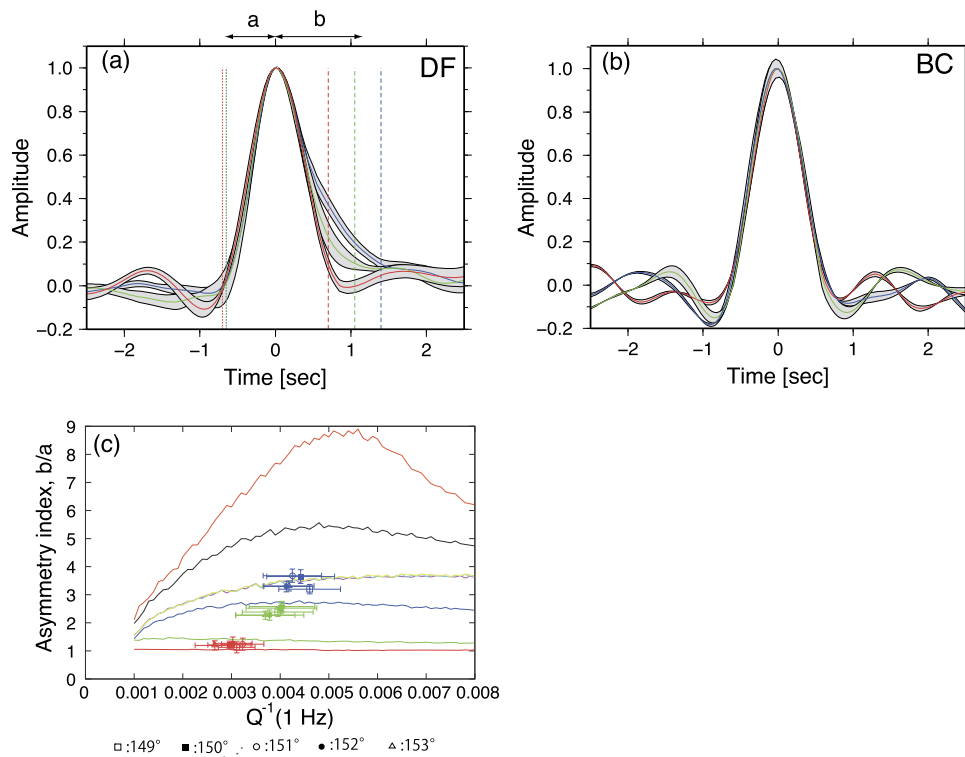


Fig. 7. (a) Stacked PKP(DF) waveforms for the eastern hemisphere (blue line), W1 (red), and W2 (green). PKP(DF) phases are deconvolved with the reference waveforms for each event, and then stacked along measured traveltimes for each sampling region. Shade indicates one standard error region, and vertical lines denote timings of 10% of the peak amplitude. To avoid the contamination of PKP(BC) phase, waveforms in which PKP(DF) phase is well separated from PKP(BC) phase (distance > 147°) are used for calculating stacked waveforms. (b) Similar to (a) but for stacked PKP(BC) waveforms. Note that there is no systematic difference for different regions. (c) Asymmetry indexes and $Q^{-1}_{1\text{Hz}}$ of theoretical impulse response functions and the observed stacked waveforms are compared. Colors for lines are the same as in Fig. 1b–d, and colors in estimated points of symbols are the same as in (a). Note that lines for $\tau_1 = 10^1, 10^2, 10^3$ overlay each others. Error bars denote one standard errors. (For interpretation of the references to color in this figure, the reader is referred to the web version of this article.)

eastern hemisphere and thus can be consistent with frequency independent attenuation if an appropriate correction for the P-wave velocity is applied.

Our result is partly consistent with that of Li and Cormier (2002) who reported frequency dependent attenuation without hemispherical difference, but not for the eastern hemisphere. We may be able to attribute this partly to the difference in the distance range of analyses (their analysis is for the deeper structure) and partly to the difference of analyzed waveforms (first half-cycle of velocity vs. full-cycle of displacement).

4.2. Effect of absorption band width

We have so far considered cases with fixed $\tau_1/\tau_2 = 10^5$. As the band width of seismic observation is quite limited (0.02–2 Hz), this restriction has almost no effect on the result (Li and Cormier, 2002) unless the absorption peak is narrow. To investigate such an effect of the absorption band width, we consider cases of $\tau_1/\tau_2 = 10^1, 10^2$, and perform the same analysis as for $\tau_1/\tau_2 = 10^5$ case. The results are compared in Fig. 9. The misfit in the first row corresponds to an average of L1-norm of misfit for each event–array pair normalized by L1-norm of observed seismograms:

$$\text{misfit} = \text{average} \left(\frac{\sum_i |u_i(t) - s_i(t)|}{\sum_i |u_i(t)|} \right),$$

where $u_i(t)$ and $s_i(t)$ are observed and synthetic waveforms of i -th record of an event–array pair, respectively.

The result indicates that some of narrow band models fit the data as good as those best models of $\tau_1/\tau_2 = 10^5$ case. If we plot absorption spectra of those acceptable models (second and third rows of Fig. 9), what is really resolved becomes clearer. For the

eastern hemisphere, flat (frequency independent) attenuation and strong velocity dispersion in the whole analysis frequency band is required by data, and thus absorption band must be wider than $\tau_1/\tau_2 = 10^2$. For W1, opposite, frequency dependent attenuation and weak velocity dispersion is required. Although there is no constraint on the band width, the peak must reside outside of the analysis frequency band. For W2, the situation appears to be the between. What appears to be required is that the lowest corner frequency resides within the analysis band, and a slight velocity dispersion exists in the higher half of the frequency band (above 0.2 Hz). So this test confirms the basic characteristics of preferred models for each region resolved in the previous section (e.g., Fig. 6).

4.3. Absorption band model for intricate quasi-hemispherical heterogeneity

The quasi-hemispherical pattern of the frequency dependence of attenuation revealed in this study appears to have a strong connection with the pattern of the attenuation and velocity profiles resolved in paper 1 (Fig. 4b, c): i.e., the frequency independent attenuation occurs in a region with high attenuation and fast velocity at 1 Hz as in the eastern hemisphere, and the frequency dependent attenuation occurs in a region with low attenuation and slow velocity as in the western hemisphere (Table 1). Here, we try to explain these features in terms of the frequency range of seismic observation and the location of the absorption band in frequency domain. In Fig. 10a, possible relative positions of the analysis frequency range for each studied region and an absorption band model are shown. In the eastern hemisphere, the analysis frequency range (0.02–2.0 Hz) may coincide with the absorption band peak frequency range that exhibits strong but

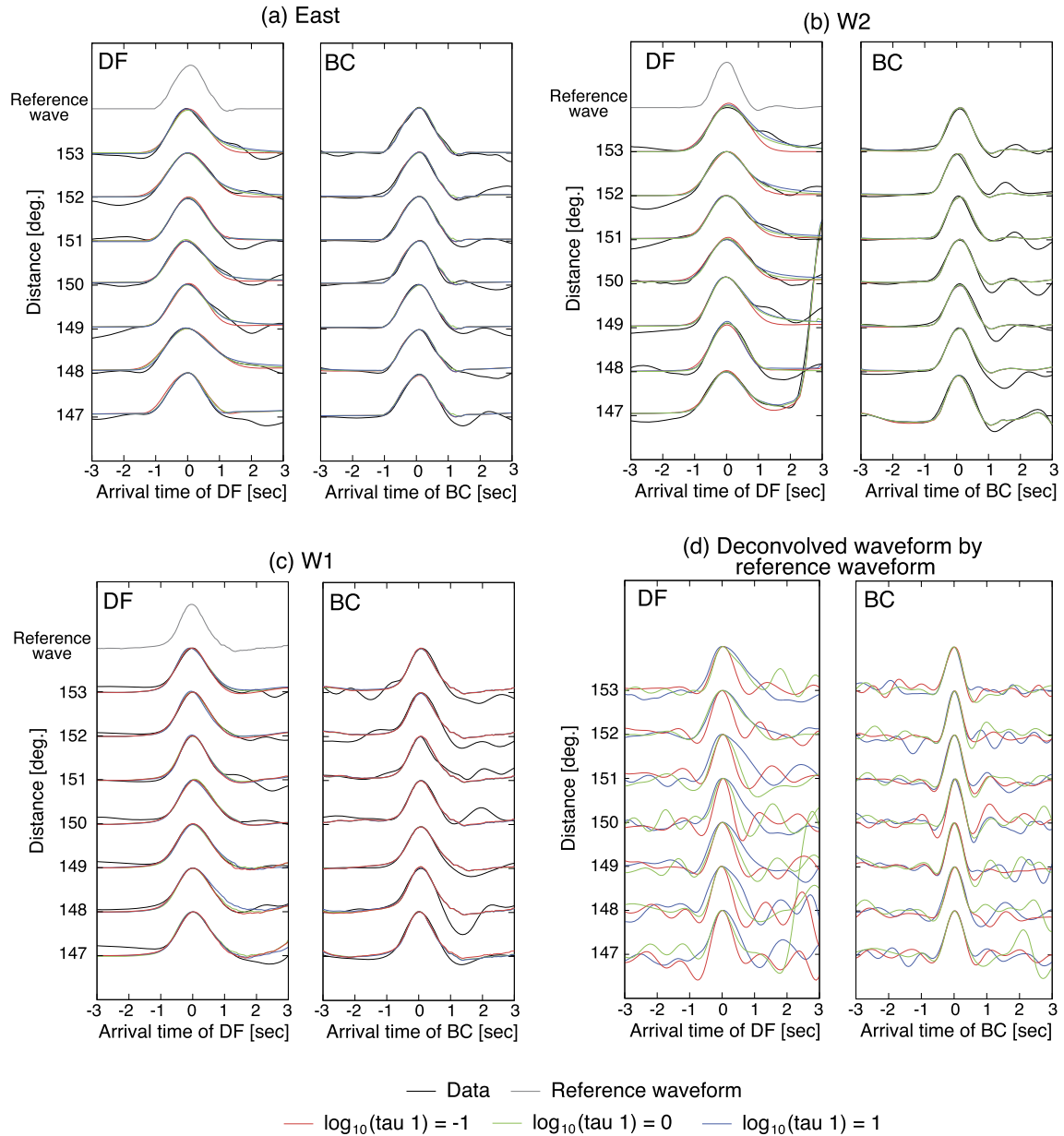


Fig. 8. ((a)–(c)) Comparison of individual waveforms of observed and modeled PKP(DF) and PKP(BC) phases for events that sample the eastern hemisphere (a) (event: 15 Aug. 2006 in Fiji), W2 (b) (30 Sep. 2009 in South America), and W1 (c) (11 Apr. 2005 in South America). Observed waveforms are shown in black, and model waveforms obtained by using $\tau_1 = 10^{-1}$, $\tau_1 = 10^0$ and $\tau_1 = 10^1$ in the waveform inversion are colored in red, green and blue, respectively. The reference waveforms, $W(t)$, which are essentially identical for different τ_1 values, are plotted at the top of DF waveforms. Waveforms are normalized by amplitudes of PKP(DF) and PKP(BC) of observed data. (d) Observed PKP(DF) and PKP(BC) waveforms in (a)–(c) deconvolved by corresponding reference waveforms are shown. Different colors here indicate different regions as in Fig. 7a. All waveforms are aligned by the measured traveltime of each phase. (For interpretation of the references to color in this figure legend, the reader is referred to the web version of this article.)

frequency independent attenuation and strong dispersion. In the western hemisphere, W1 and the shallower part of W2, the analysis frequency range may reside far outside of the absorption band where weak but frequency dependent attenuation, and slow but constant velocity are expected. Finally in the deeper part of W2, the situation might be between above two cases, i.e., the analysis frequency range may be located near the lower corner of the absorption band where frequency dependent but relatively strong attenuation, and slow but weak dispersion are expected (such an interpretation also explains the observation of the large difference in the attenuation but small difference in the velocity between W1 and W2 in the depth range 150–300 km). Fig. 10b illustrates these relationships in the absolute frequency frame, in which the seismic frequency band resides between 0.02 and 2.0 Hz, and the absorp-

tion models for three regions are shifted relative to each other in frequency.

The positive correlation between attenuation and seismic velocity variations in the inner core (i.e., strong (weak) attenuation and fast (slow) velocity coincide), often based on observations in narrow frequency bands, has been considered as a line of supporting evidence for scattering as the cause of the attenuation in the inner core (e.g., Souriau, 2003; Monnereau et al., 2010). The absorption band model of our broadband observation presented here, however, makes us to reconsider such a simple interpretation, although it does not necessarily exclude the scattering hypothesis. We, therefore, consider both intrinsic viscoelastic attenuation and scattering attenuation as possible scenarios to explain the observa-

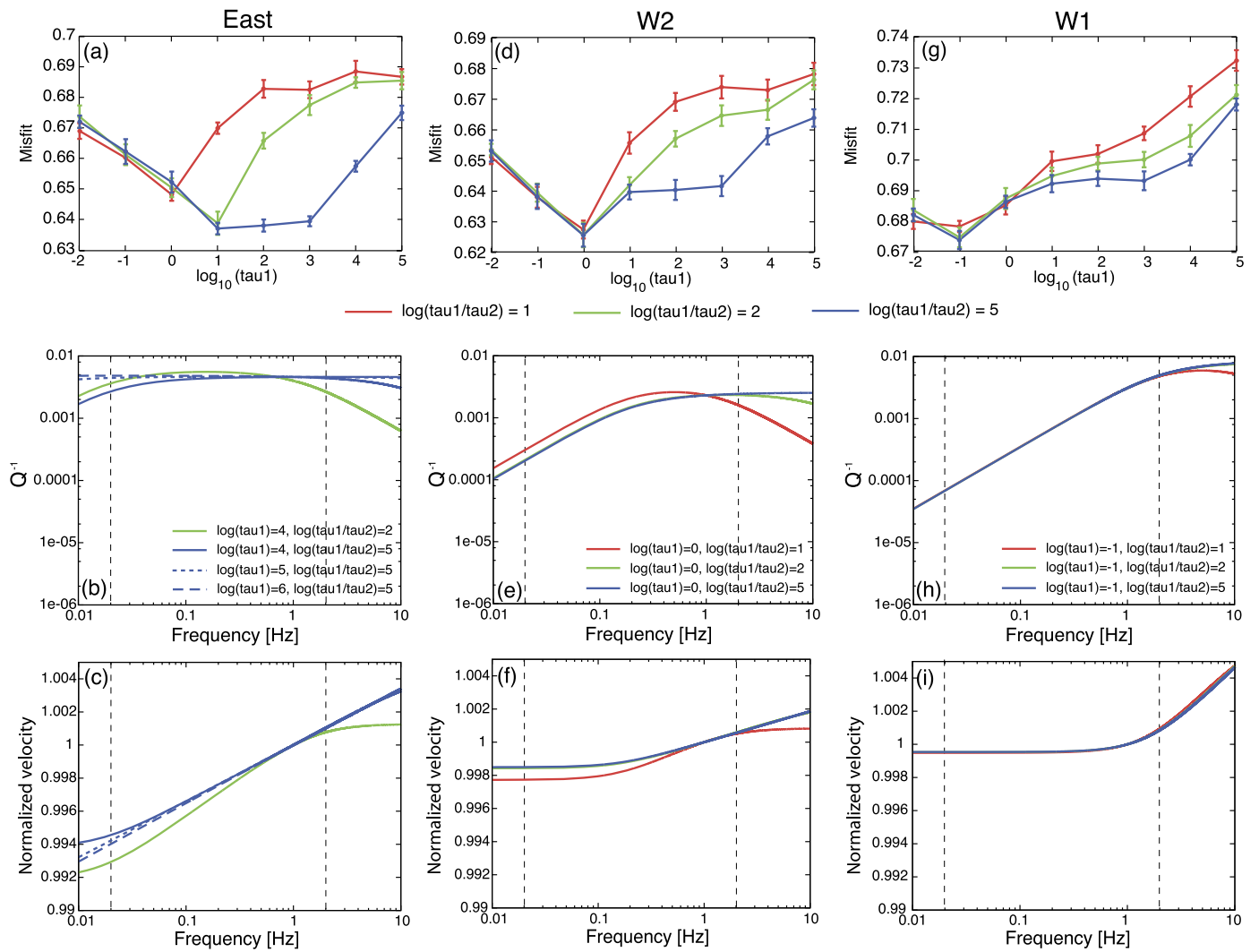


Fig. 9. The results of analysis with different absorption band width models ($\tau_1/\tau_2 = 10^1, 10^2, 10^5$) for the eastern hemisphere ((a)–(c)), the western hemisphere, W2 ((d)–(f)), and W1 ((g)–(i)). The first row ((a), (d), (g)) shows the L1 norm misfits for different τ_1 models; the second row ((b), (e), (h)) and the third row ((c), (f), (i)) show absorption spectra (Q^{-1} , velocity dispersion) for the best (minimum misfit) absorption models seen in the first row for three regions. Broken lines indicate the frequency range of the analysis.

Table 1

Summary of obtained features of the attenuation and velocity in paper 1 and frequency dependence of the attenuation in this study for the top 300 km of the inner core.

	East	West	
		W2	W1
Attenuation	High \rightarrow Low (Shallow \rightarrow Deep)	Low \rightarrow High (Shallow \rightarrow Deep)	Low
Velocity	Fast	Slow	Slow
Frequency dependence of the attenuation	Independent	Partially dependent	Dependent
Grain size	Large (>30 km) \rightarrow Moderate	Small \rightarrow Moderate	Small
Temperature	Low \rightarrow Moderate	High \rightarrow Moderate	High

4.3.1. Scattering scenario for grain size variation

The absorption band model for seismic attenuation is conventionally employed to account for the intrinsic attenuation (e.g., Li and Cormier, 2002; Anderson, 1989). Considering the well established observations for the presence of strong scatterers in the inner core (e.g., Vidale and Earle, 2000; Leyton and Koper, 2007), however, here we attempt to interpret our observation in terms of attenuation due to scattering with variable grain sizes. It has been suggested that the strongest attenuation occurs when the seismic wavelength is comparable to the grain size (Cormier and Li, 2002;

Calvet and Margerin, 2008). If the dominant grain size has a certain range (a range of an order or so) in a self-similar manner, the corresponding attenuation spectrum is likely to have a flat peak similar to that of the absorption band model. Considering that seismic observation band is limited (0.02–2.0 Hz), a peak width of two orders of magnitude in frequency is the resolution limit of analysis (e.g., Li and Cormier, 2002), and a range of one order of dominant grain size variation may satisfy the condition (e.g., Cormier and Li, 2002; Calvet and Margerin, 2008). If such is the case, the result schematically summarized in Fig. 10b may be interpreted in terms

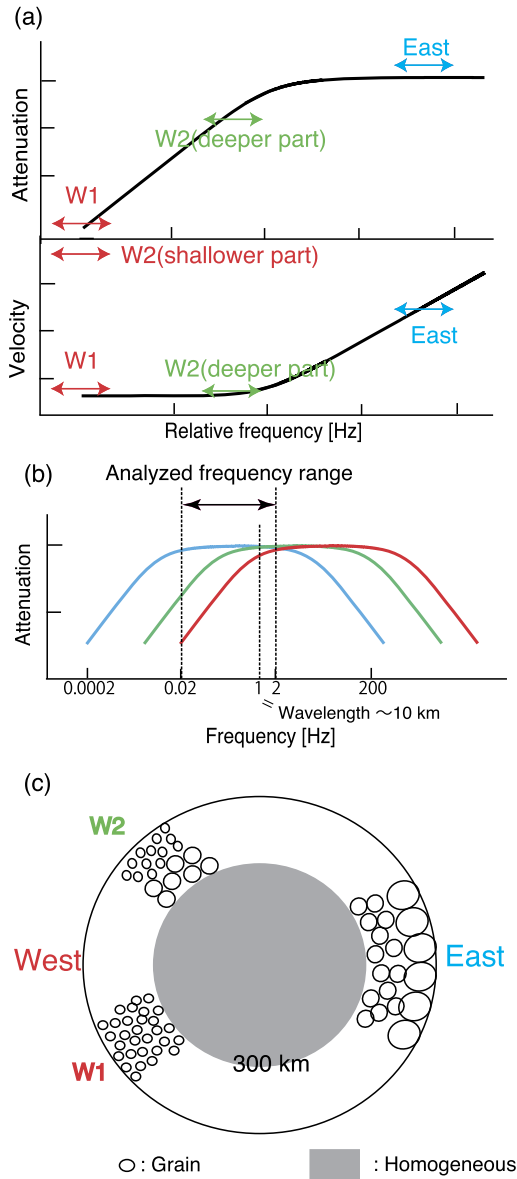


Fig. 10. (a) Relative positions of the seismic analysis frequency range for each region in the absorption band model spectrum (top) and in the corresponding dispersion curve (bottom). (b) Absorption spectra for three regions are schematically shown in the absolute frequency frame: red, green, and blue lines represent W1 and the shallower part of W2 (ICB–150 km), the deeper part of W2 (150–300 km), and the eastern hemisphere, respectively. (c) Schematic figure showing the distribution of the grain size of iron crystals inferred by the scattering scenario, which represents one of the possible scenarios. Shadow indicates a homogeneous area inferred in paper 1. (For interpretation of the references to color in this figure, the reader is referred to the web version of this article.)

of the grain size variation for the studied regions: the position of the attenuation peak shifts to higher frequency as the grain size becomes smaller.

In this scenario, which still needs to be fully tested by the waveform analysis with appropriate scattering models (e.g., Cormier and Li, 2002; Calvet and Margerin, 2008), based on the assumption that attenuation is strongest at a wavelength, λ , comparable to the dominant grain size, d , ($d \sim \lambda/\pi$, Calvet and Margerin (2008)), the grain size of the top 150 km of the eastern hemisphere may be estimated to be significantly larger than 30 km (blue line in Fig. 10b). For other regions, peaks are located at higher frequency range (red and green lines in Fig. 10b), and thus smaller dominant grain sizes are expected. Fig. 10c shows a schematic

picture of the distribution of grain size that might be inferred from these arguments. The frequency dependence of attenuation studied in this paper, together with the regional 1-D profiles of attenuation and velocity obtained in paper 1 (Fig. 4b, c), is now translated into regional and depth variation of the grain size of iron crystals.

As a model to explain the hemispherical heterogeneity of the inner core, Monnereau et al. (2010) and Alboussière et al. (2010) proposed a translational convection model of iron crystals of the inner core that crystallize in the western hemisphere side and melt (out to the outer core) in the eastern hemisphere side. Monnereau et al. (2010) further suggested that the hemispherical heterogeneity of the attenuation can be explained by the difference in the grain size, and that the grain size changes from 50 m at the crystallizing side (the western hemisphere) to 20 km at the melting side (the eastern hemisphere). The intricate heterogeneity and the depth variation of the grain size of the inner core inferred in this scenario may imply a regional difference in the rate of crystallization: the rate of crystallization for W1 may be slower than that for W2.

4.3.2. Viscoelastic scenario for temperature/grain-size variation

In the viscoelastic interpretation of absorption band models, it is common to assume that the relaxation processes are thermally activated and follow the Arrhenius law (e.g., Nowick and Berry, 1972). In our case, the relaxation time parameters $\tau_{1,2}$ define the absorption band, and, assuming that some process at the grain boundary is the cause of attenuation, may be written as

$$\tau_{1,2}^{-1} \propto d^{-n} e^{-E_{\alpha}/k_B T},$$

where T is the absolute temperature, E_{α} is the activation energy, k_B is the Boltzmann constant, d is the grain size, and the index n ranges between 1 and 3 (e.g., McCarthy et al., 2011; Karato, 2012).

With this description, larger T gives smaller relaxation time, and thus larger relaxation frequency. Thus an increase in temperature results in a shift of absorption band to higher frequency. In this scenario, the eastern hemisphere of the inner core is associated with a cold temperature, while the regions in the western hemisphere are with warmer ones. This pattern is consistent with the prediction of another school of models to account for the seismologically observed quasi-hemispherical heterogeneities that attribute them to the thermal heterogeneity at the bottom of the mantle (Sumita and Olson, 1999; Aubert et al., 2008; Gubbins et al., 2011). Thus, the viscoelastic scenario with temperature variation leads to a colder and crystallizing eastern hemisphere and warmer and melting regions of the western hemisphere, which is the opposite of what the scattering scenario does. Considering the recent finding of high thermal conductivity of iron in the core (e.g., Pozzo et al., 2012), however, a large temperature variation in the inner core may not be expected, and thus this scenario may not be effective.

The viscoelastic scenario with grain size variation, on the other hand, predicts that a shift of absorption band to higher frequency occurs for a smaller grain size, a qualitatively similar pattern to the effect of scattering. So regardless the scenarios, grain size variation as the origin of the absorption band model seems to be consistent with the pattern predicted by the translational convection model (Monnereau et al., 2010).

4.3.3. Viscoelastic vs. scattering?

By analyzing PKiKP coda decay rates in a frequency range of 2–5 Hz, Leyton and Koper (2007) found evidence for laterally varying volumetric (back)scattering in the upper inner core. Considering that the analysis frequency ranges do not overlap each other, their result neither contradicts nor is consistent with our observation, but the absorption band model shown in Fig. 10b may need

to be carefully examined. They showed evidence for strong scattering from the Pacific Ocean and Asia in the eastern hemisphere, and this can be consistent with the model if the higher cut frequency is located above 5 Hz. However, their relatively few observations of scattering coming from the Atlantic Ocean (W1), if it means weak scattering in the region, it may not be consistent with the model (the red line in Fig. 10b). We also note that the scattering scenario requires the presence of fairly large (>30 km) scatters for the shallow part of the eastern hemisphere. Considering these points, it seems difficult that the scattering scenario by itself fully explains the observation.

The reality may be that both viscoelastic and scattering attenuation scenarios coexist (e.g., Leyton and Koper, 2007; Cormier and Attanayake, 2013), with one possibly dominating in some regions/scales and the other in other regions/scales. Also the viscoelastic scenario should include effects of melt with appropriate geometrical considerations (e.g., Singh et al., 2000; Takei, 2002; Sumita and Bergman, 2006). What seems now important is to quantify contributions of various mechanisms for the inner core attenuation both theoretically and observationally. For example, how different mechanisms, when their parameters such as amount of melt or grain size vary, affect the absorption band model, either by shifting in frequency or by changing the peak attenuation value, Q_m^{-1} , is quantified, what mechanism is dominating may be delineated, as our observation appears to favor a shift in frequency rather than a change in Q_m^{-1} , although the constraint is not so strong (Figs. 6 and 9).

5. Conclusion

Via the nonlinear waveform inversion method that incorporates the frequency dependence of attenuation, we systematically model broadband (0.02–2 Hz) core phases recorded by global seismic arrays, and reveal that attenuation is frequency independent in the quasi-eastern hemisphere and frequency dependent in the quasi-western hemisphere of the inner core. This observation, together with our reported quasi-hemispherical heterogeneity of seismic velocity and attenuation at ~ 1 Hz, can be understood in terms of the absorption band model of attenuation whose peak frequency range shifts to higher frequency from the quasi-eastern hemisphere to the quasi-western hemispheric regions (from W1 to W2). If we attribute this solely to the grain size variation of iron crystal in the inner core, regardless of the attenuation mechanism (either scattering or viscoelastic), the grain size is predicted to be smaller in the western hemisphere than in the eastern hemisphere, a pattern consistent with the translational convection model of the inner core evolution. We must not, however, over-interpret this, until contribution of other mechanisms for the inner core attenuation, such as the effect of melt, is fully quantified.

Acknowledgements

We thank all the participants of the NECESSArray project, and staff of IRIS, NIED, and ORFEUS data center for providing high-quality broadband seismic data. Constructive comments by the referees, Vernon Cormier and Hrvoje Tkaličić, and the editor, Peter Shearer were helpful to improve the manuscript. We also thank S. Tanaka, H. Shimizu, Y. Takei and I. Sumita for helpful discussions. The Generic Mapping Tools (Wessel and Smith, 1998) is used to draw some of the figures, and the Taup softwares (Crotwell et al., 1999) are used for the calculation of theoretical traveltimes. This work was supported by Grant-in-Aids for JSPS Fellows (23-10283) and by Grant-in-Aid for Scientific Research 19104011 provided by JSPS.

Appendix A. Supplementary material

Supplementary material related to this article can be found online at <http://dx.doi.org/10.1016/j.epsl.2014.08.038>.

References

- Alboussi re, T., Deduen, R., Melzani, M., 2010. Melting induced stratification above the Earth's inner core due to convective translation. *Nature* 466, 744–747.
- Anderson, D.L., 1989. Anelasticity. In: *Theory of the Earth*. Blackwell, pp. 279–302 (Chapter 14).
- Attanayake, J., Cormier, V.F., deSilva, S.M., 2014. Uppermost inner core seismic structure – new insights from body waveform inversion. *Earth Planet. Sci. Lett.* 385, 49–58.
- Aubert, J., Amit, H., Hulot, G., Olson, P., 2008. Thermochemical flows couple the Earth's inner core growth to mantle heterogeneity. *Nature* 454, 758–761.
- Bhattacharyya, J., Shearer, P., Masters, G., 1993. Inner core attenuation from short-period PKP(BC) versus PKP(DF) waveforms. *Geophys. J. Int.* 114, 1–11.
- Calvet, M., Margerin, L., 2008. Constraints on grain size and stable iron phases in the uppermost inner core from multiple scattering modeling of seismic velocity and attenuation. *Earth Planet. Sci. Lett.* 228, 243–253.
- Cao, A., Romanowicz, B., 2004. Hemispherical transition of seismic attenuation at the top of the Earth's inner core. *Earth Planet. Sci. Lett.* 228, 243–253.
- Chevrot, S., 2002. Optimal waveform and delay time analysis by simulated annealing. *Geophys. J. Int.* 151, 164–171.
- Cormier, V.F., Attanayake, J., 2013. Earth's solid inner core: seismic implications of freezing and melting. *J. Earth Sci.* 24, 683–698. <http://dx.doi.org/10.1007/s12583-013-0363-9>.
- Cormier, V.F., Li, X., 2002. Frequency-dependent seismic attenuation in the inner core: 2. A scattering and fabric interpretation. *J. Geophys. Res.* 107, 2362.
- Cormier, V.F., Li, X., Choy, G.L., 1998. Seismic attenuation of the inner core: viscoelastic or stratigraphic? *Geophys. Res. Lett.* 25, 4019–4022.
- Cormier, V.F., Richards, P.G., 1988. Spectral synthesis of body waves in Earth models specified by vertically varying layers. In: Doornbos, D.J. (Ed.), *Seismological Algorithms*. Academic Press, pp. 1–45.
- Crotwell, H.P., Owens, T.J., Ritsema, J., 1999. The TauP toolkit: flexible seismic travel-time and ray-path utilities. *Seismol. Res. Lett.* 70, 154–160. <http://dx.doi.org/10.1785/gssrl.70.2.154>.
- Cummins, P., Johnson, L.R., 1988. Short-period body wave constraints on properties of the Earth's inner core boundary. *J. Geophys. Res.* 93, 9058–9074.
- Doornbos, D.J., 1983. Observable effects of the seismic absorption band in the Earth. *Geophys. J. R. Astron. Soc.* 75, 693–711.
- Dziewonski, A., Anderson, D.L., 1981. Preliminary reference Earth model. *Phys. Earth Planet. Inter.* 25, 297–356.
- Garcia, R., Chevrot, S., Weber, M., 2004. Nonlinear waveform and delay time analysis of triplicated core phases. *J. Geophys. Res.* 109, B01306.
- Garcia, R., Tkal ci c, H., Chevrot, S., 2006. A new global PKP data set to study the Earth's core and deep mantle. *Phys. Earth Planet. Inter.* 159, 15–31.
- Gubbins, D., Sreenivasan, B., Mound, J., Rost, S., 2011. Melting of the Earth's inner core. *Nature* 473, 361–364. <http://dx.doi.org/10.1038/nature10068>.
- Iritani, R., Takeuchi, N., Kawakatsu, H., 2010. Seismic attenuation structure of the top half of the inner core beneath the northeastern Pacific. *Geophys. Res. Lett.* 37, L19303.
- Iritani, R., Takeuchi, N., Kawakatsu, H., 2014. Intricate heterogeneous structures of the top 300 km of the Earth's inner core inferred from global array data: I. Regional 1D attenuation and velocity profiles. *Phys. Earth Planet. Inter.* 230, 15–27.
- Kaelin, B., Johnson, L.R., 1998. Dynamic composite elastic medium theory. Part II. Three-dimensional media. *J. Appl. Phys.* 84, 5458–5468. <http://dx.doi.org/10.1063/1.368308>.
- Kaneshima, S., Hirahara, K., Ohtaki, T., Yoshida, Y., 1994. Seismic structure near the inner core–outer core boundary. *Geophys. Res. Lett.* 21, 157–160.
- Karato, S.I., 2012. Physical mechanisms of seismic wave attenuation. In: *Deformation of Earth Materials*. Cambridge Univ. Press, pp. 199–213 (Chapter 11).
- Kawai, K., Geller, R.J., Fuji, N., 2007. D'' beneath the Arctic from inversion of shear waveforms. *Geophys. Res. Lett.* 34, L21305.
- Leyton, F., Koper, K.D., 2007. Using PKiKP coda to determine inner core structure: 2. Determination of Q_c . *J. Geophys. Res.* 112, B05317. <http://dx.doi.org/10.1029/2006JB004370>.
- Li, X., Cormier, V.F., 2002. Frequency-dependent seismic attenuation in the inner core: 1. A viscoelastic interpretation. *J. Geophys. Res.* 107, 2361.
- Liu, H.P., Anderson, D.L., Kanamori, H., 1976. Velocity dispersion due to anelasticity; implications for seismology and mantle composition. *Geophys. J. R. Astron. Soc.* 47, 41–58.
- McCarthy, C., Takei, Y., Hiraga, T., 2011. Experimental study of attenuation and dispersion over a broad frequency range: 2. The universal scaling of polycrystalline materials. *J. Geophys. Res.* 116, B09207. <http://dx.doi.org/10.1029/2011JB008384>.
- Monnerau, M., Calvet, M., Margerin, L., Souriau, A., 2010. Lopsided growth of Earth's inner core. *Science* 328, 1014–1017.

- Nowick, A.S., Berry, B.S., 1972. *Anelastic Relaxation in Crystalline Solids*. Academic Press.
- Pozzo, M., Davies, C., Gubbins, D., Alfe, D., 2012. Thermal and electrical conductivity of iron at Earth's core conditions. *Nature* 485, 355–358.
- Singh, S.C., Taylor, M.A.J., Montagner, J.P., 2000. On the presence of liquid in Earth's inner core. *Science* 287, 2471–2474.
- Souriau, A., 2003. The seismological picture of the inner core: structure and rotation. *C. R. Géosci.* 335, 51–63.
- Souriau, A., 2009. Inner core structure: constraints from frequency dependent seismic anisotropy. *C. R. Géosci.* 341, 439–445.
- Souriau, A., Roudil, P., 1995. Attenuation in the uppermost inner core from broadband GEOSCOPE PKP data. *Geophys. J. Int.* 123, 572–587.
- Sumita, I., Bergman, M.I., 2006. Inner-core dynamics. In: *Treatise on Geophysics*, vol. 8, pp. 299–318.
- Sumita, I., Olson, P., 1999. A laboratory model for convection in Earth's core driven by a thermally heterogeneous mantle. *Science* 286, 1547–1549.
- Takei, Y., 2002. Effect of pore geometry on V_P/V_S : from equilibrium geometry to crack. *J. Geophys. Res.* 107, B2. <http://dx.doi.org/10.1029/2001JB000522>.
- Tanaka, S., 2012. Depth extent of hemispherical inner core from PKP(DF) and PKP(Cdiff) for equatorial paths. *Phys. Earth Planet. Inter.* 210–211, 50–62.
- Tanaka, S., Hamaguchi, H., 1997. Degree one heterogeneity and hemispherical variation of anisotropy in the inner core from PKP(BC)–PKP(DF) times. *J. Geophys. Res.* 102, 2925–2938.
- Vidale, J.E., Earle, P.S., 2000. Fine-scale heterogeneity in the Earth's inner core. *Nature* 404, 273–275.
- Wen, L., Niu, F., 2002. Seismic velocity and attenuation structures in the top of the Earth's inner core. *J. Geophys. Res.* 107 (B11), 2273.
- Wessel, P., Smith, H.W.F., 1998. New, improved version of the Generic Mapping Tools released. *Eos Trans. AGU* 79, 579.
- Yu, W., Wen, L., 2006. Seismic velocity and attenuation structures in the top 400 km of the Earth's inner core along equatorial paths. *J. Geophys. Res.* 111, B07308.